Near global scale high-resolution seasonal simulations with WRF-NOAHMP v.3.8.1

Thomas Schwitalla[1], Kirsten Warrach-Sagi[1], Volker Wulfmeyer[1], Michael Resch[2]

[1]Institute of Physics and Meteorology, University of Hohenheim, Stuttgart, 70599, Germany

5 [2]High-Performance Computing Center Stuttgart, Stuttgart, Germany

Correspondence to: Thomas Schwitalla (thomas.schwitalla@uni-hohenheim.de)

Abstract. The added value of global simulations on the convection-permitting (CP) scale is a subject of extensive research in the earth system science community. An increase in predictive skill can be expected due to advanced representations of feedbacks and teleconnections in the ocean-land-atmosphere system. However, the proof of this

10 hypothesis by corresponding simulations is computationally and scientifically extremely demanding. We present a novel latitude-belt simulation from 57° S to 65° N using the WRF-NOAHMP model system with a grid increment of 0.03° over a period of 5 months forced by sea surface temperature observations. In comparison to a latitude-belt simulation with 45 km resolution, at CP resolution the representation of the spatial-temporal scales as well as the organization of tropical convection are improved considerably. The teleconnection pattern are very close to that of

15 the operational ECMWF analyses. The CP simulation is associated with an improvement of the precipitation forecast over South America, Africa, and the Indian Ocean and considerably improves the representation of cloud coverage along the tropics. Our results demonstrate a significant added value of future simulations on the CP scale up to the seasonal forecast range.

1 Introduction

20 The answer whether global simulations on the convection permitting (CP) scale is computational overkill or not, will not only have substantial consequences for the future direction of earth system sciences but also with respect to the realization and distribution of huge resources on supercomputers. This requires the involvement of decision makers, funding organizations, and the public.

Extensive research is ongoing concerning the added value of global extended range simulations on the CP scale.

25 These simulations are considered for next generation climate projections (Eyring et al., 2016), seasonal forecasting (Vitart, 2014), and numerical weather prediction (NWP). We hypothesize that the skill for simulating extremes such as droughts and extreme precipitation (Bauer et al., 2015) is improved, which is critical for decision makers, disaster and water management as well as food and water security. However, the huge investment in the required computational resources is challenging.

30 So far, global CP simulations were limited to a forecast range of a few days or weeks (Miyamoto et al., 2013; MIYAKAWA and MIURA, 2019; Satoh et al., 2019) which is usually too short for agricultural applications and thus enhancing e.g. food security. On longer time scales, CP simulations are only available using limited area models (LAMs) (Hagelin et al., 2017). However, LAMs are strongly affected by the lateral boundaries. For instance, regional climate projections, which are still operated with grid increments of approx. 10-20 km, show a

strong influence of the driving global model on regional surface temperature statistics (Kotlarski et al., 2014) while the precipitation statistics is mainly influenced by the parameterization of deep convection (Prein et al., 2013; Prein et al., 2015) in the regional models.

Downscaling of global climate projections as well as seasonal forecast and NWP model ensembles on the CP scale (Bouttier et al., 2016; Fosser et al., 2015; Kendon et al., 2014; Stratton et al., 2018; Warrach-Sagi et al., 2013) indicated an added value with respect to extreme precipitation statistics. However, these efforts did not allow for studying the added value of global CP ensembles without zonal lateral boundaries avoiding additional errors by the global driving models (Žagar et al., 2013).

In this study, the added value of a CP resolution WRF simulation is compared to a 0.45° resolution by means of ECMWF analyses and satellite observations. The simulation period of five months allows for studying the simulation of the organization and lifetime of tropical precipitation as well as for investigating teleconnection patterns.

This study can be considered as an extension of the work of Schwitalla et al. (2017) who performed a convection permitting latitude belt simulation on a shorter time scale and smaller domain.

The manuscript is organized as follows: Section 2 provides details about the experimental setup, technical details, and the validation strategy. Sections 3.1 and 3.2 describe the results with respect to tropical convection, followed analysing global cloud, precipitation, and teleconnection patterns. Section 4 summarizes our results.

2 Experimental setup

2.1 Model setup

For the experiment, two simulations with a 5-month forecast range from February to June 2015 were carried out using version 3.8.1 of the WRF-NOAHMP model system (Skamarock et al., 2008). This period was a strong El Niño year (Newman et al., 2018) with large Sea Surface Temperature (SST) anomalies along the El Niño 3.4 region. The simulations covered a latitude belt between 57° S and 65° N with a grid increment of 0.03 degrees (CP run) and 0.45 degrees (NCP run) grid increments, respectively (Fig. 1).

The reasons to choose this particular region manyfold: 1) The main focus of our work is on tropical convection, 2) applying the WRF model in polar regions requires a special setup of the physical parametrizations (Bromwich et al., 2018; Hines and Bromwich, 2017), and 3) the applied regular latitude-longitude grid leads to very high map-scale factors beyond 65° latitude thus enforcing a very short model integration time step.

The WRF model is based on an Arakawa-C grid and utilizes a terrain following vertical coordinate system with 57 levels up to 10 hPa in our simulations. 15 out of 57 levels represented the lowest 1500 above ground level (AGL). Both resolutions shared a common physics package. The applied physics schemes are the NOAH-MP land surface model (Niu et al., 2011), which predicts soil moisture and temperature in four different depths as well as includes a 3-layer snow model and the Jarvis scheme for vegetation (Jarvis, 1976). For the WRF physics, we chose the

revised MM5 similarity surface layer scheme based on Monin-Obukhov similarity theory (MOST) (Jiménez et al., 2012), the YSU boundary layer parametrization (Hong, 2010), the GRIMS shallow cumulus scheme (Hong et al., 2013), and the Rapid Radiative Transfer Model for GCMs (RRTMG) for shortwave and longwave radiation (Iacono et al., 2008). In order to improve the radiative transfer calculations, aerosol optical depth (AOD) data from the Monitoring Atmospheric Composition and Climate (MACC) analysis (Inness et al., 2013) were used. The AOD interacts with the RRTMG shortwave radiation scheme so that an improvement in the simulation of surface temperatures can be expected. For cloud and precipitation microphysics, the Thompson 2-moment scheme (Thompson et al., 2008) with five categories of hydrometeors was applied. The prescribed value of the cloud droplet number concentration in the Thompson microphysics scheme was changed from the default value of 100×10^6 m^{-3} for maritime cases to 200×10^6 m^{-3}. This describes an intermediate aerosol loading which appears to be more realistic in case of continental convection (Heikenfeld et al., 2019). In this setup, no direct aerosol interaction of radiation and cloud microphysics takes place and the cloud droplet number concentrations remains constant throughout the model domain. Deep convection was parametrized by the Grell-Freitas scheme (Grell and Freitas, 2014) and is only applied in the NCP simulation. The model integration time-step was set to 10 s for the CP and 150 s for the NCP simulation, respectively. Output of the most important surface variables is available every 30 min.

For the land use maps, a combined product of IGBP-MODIS and CORINE data bases was applied which provided an advanced representation of land cover. Instead of the coarse FAO soil texture data available in the WRF package, data from the Harmonized World Soil Data Base were used with a resolution of 1 km (Milovac et al., 2014) . Terrain information was provided by the more recent Global Multi-resolution Terrain Elevation Data 2010 (GMTED2010) data set.

The initial conditions and forcing data at the meridional boundaries were taken from the operational European Centre for Medium Range Weather Forecasting (ECMWF) analysis every 6 hours at a resolution of 0.125°, as obtained from the Meteorological Archival and Retrieval System (MARS).

Although e.g. Mogensen et al. (2017) found a superior tropical cyclone forecasting performance in case the Nucleus for European Modelling of the Ocean (NEMO) model (Madec, 2008) was applied in the ECMWF operational model, we decided to apply updated observed SSTs in our simulation to obtain a surface forcing over water surfaces to investigate the added value of the CP resolution.

SST data were provided by a combining the operational ECMWF SST analysis with the Operational Sea Surface Temperature and Sea Ice Analysis (OSTIA) system of the UK MetOffice (Donlon et al., 2012) available at a horizontal resolution of 0.05°. In order to match the six hourly atmospheric boundary conditions, the SST data were interpolated in time. This approach still provided reasonable feedback towards the atmosphere via coupling with the applied surface layer scheme. This scheme updates the surface fluxes, the exchange coefficients for heat and moisture, and the friction velocity depending on the environmental conditions as input for the PBL parametrization.

As both SST data sets have different land-sea masks, certain inland lakes are resolved only in the ECMWF or the OSTIA data sets. In order to combine their information, changes of the WRF code were necessary. Firstly, we implemented a check for water points whether an SST from OSTIA was available due to its higher resolution. If

this was true, the ECMWF SST was discarded at the corresponding grid cell. In case no SST from OSTIA but from
105 ECMWF was available, the latter one was considered. In case no SST from either ECMWF or OSTIA was available, the ECMWF surface temperature was considered instead and the lake SST was limited between 34°C and -2°C in order to avoid unrealistic surface fluxes over inland lakes. As the WRF pre-processing system (WPS) cannot handle gridded binary (GRIB) files larger than 2 GB, which was the case for the ECMWF analysis GRIB files, it was necessary to split all 3-dimensional variables from the ECMWF analysis into separate GRIB files. WPS
110 supports parallelism utilizing MPI but currently parallel NetCDF is not supported during the horizontal interpolation step. This implies that the array size per variables is limited to 4 GB. As the CP grid comprises of 12000*4060 cells and ECMWF offers 137 vertical levels, one variable would have a size of approx. 25GB, which is far beyond the serial NetCDF capabilities. Therefore, the file format option *io_form_metgrid in the namelist.wps* file requires to be set to 102 so that each MPI task wrote its own *met_em* NetCDF file. Due to the large domain and
115 memory requirements, at least 35 compute nodes with 4480 GB memory were necessary for this task, resulting in approx. 500000 files of 100 MB file size each to successfully perform the horizontal interpolation step.

The CP simulation was performed using 4096 nodes of the Hazel Hen system of the High-Performance Computing Center Stuttgart (HLRS; Bönisch et al. (2017)). This supercomputer comprises of 7712 compute nodes with 2 Intel 12-core CPU at 2.5 GHz clock frequency. Due to limitations in the I/O data rates, even when parallel NetCDF is
120 applied, the CP simulation was performed on 4096 nodes with 6 OpenMP threads per node. Approximately 17 forecast days can be simulated within 24 hours wall clock time applying a fixed model time step of 10 s at the CP scale.

Currently, the WRF model source code is not ready yet to create very large NetCDF files by default. As such a large domain requires more than 2^{32}-4 bytes for each 3-dimensional variable array, changes to the code were
125 necessary to follow the CDF-5 standard, which allows for data arrays larger than 2^{32} bytes (Schwitalla et al., 2017). The complete namelist settings are provided as supplement or can be downloaded from https://doi.org/10.5281/zenodo.3550622.

2.2. Validation data sets

The evaluation of precipitation was performed against the Global Precipitation Mission (GPM) level 3 V06B data
130 set (Huffman et al., 2019). The data are available from 60° S to 60° N from 30 min time intervals to monthly aggregated values. In our study, the hourly product as well as the monthly sum are applied. The regridding of the simulated precipitation of the NCP and CP simulations was performed by applying the Earth System Modelling Framework (ESMF) as part of the NCAR Command Language (NCL) script. The WRF curvilinear grid was interpolated to the GPM rectilinear grid by applying the conservative remapping method, which gives better results
135 in case of discontinuous variables (Kotlarski et al., 2014). The ESMF regridding routines were compiled to fully exploit the MPI capabilities resulting in a considerable speed up of the interpolation procedure.

The Wheeler-Kiladis spectra (Wheeler and Kiladis, 1999) were derived by adopting the "wkSpaceTime_3" example from NCL to the CERES top of the atmosphere outgoing longwave radiation (TOA-OLR) satellite data set (Loeb et al., 2018) and both WRF simulations in 3-h intervals between 15° S and 15° N. The data were kept on

140   their original grids in order not to lose any high-resolution information. The spectral analyses took about 61 hours on a single core and required 280 GB of memory.

To validate the behaviour of the simulated downward surface shortwave flux (SWDOWN), we applied monthly mean data from the Land Surface Analysis Satallite Application Facility (LSA-SAF) (Geiger et al., 2008). This data set is derived from Meteosat Second Generation (MSG) satellite data and is available in 30 min time intervals

145   on a 0.05°*0.05° grid. This data strongly depends on cloud coverage and thus complements the TOA-OLR evaluation.

For the EOF decomposition, the following procedure was applied: First, the six hourly raw sea level pressure output and a monthly average between 55° S and 64° N were computed. Then, the EOF algorithm provided by the NCAR command language (NCL) was applied. The data were weighted by $\sqrt{\cos\theta}$ (θ being the latitude) to compensate

150   for the grid box area and to avoid a weighting overemphasis in the Tropics. The reference data set is the six hourly ECMWF operational analysis. The evaluation of 2-m temperatures and precipitable water (PW) was performed by using the six hourly ECMWF operational analysis as a reference.

3 Results

155   **3.1 Organization and lifetime of tropical convection**

In order to investigate the lifetime and propagation of tropical precipitating systems, we utilized Hovmöller diagrams (time-longitude diagrams) (Hovmöller, 1949) between 10° S and 10° N for the observed precipitation (GPM data set) as well as for the CP and NCP simulations. The results are presented in Fig. 2.

Over the entire period, the observations show several coherent propagating systems with a lifetime of 3-4 weeks

160   (Fig. 2a), demonstrating the importance of simulations beyond a month. The GPM data show that the eastward propagation speed is typically 1100 km day^{-1}. The main origins of significant amounts of precipitation along this belt are the tropical warm pools in the Western Pacific around 158-174° E and the eastern Indian Ocean around 90°E as well as the tropical rainforest over South America around 69° W. The NCP experiment (Fig. 2c) also shows precipitation maxima over the Tropical warm pools but their amplitudes are strongly overestimated. At the

165   precipitation maximum over South America, a dry zone in precipitation is simulated and second one appears around 20-25° E in strong discrepancy with the observations. The precipitation maximum over South America was shifted to approx. 35° W which corresponding to an eastward displacement of approx. 3800 km. Furthermore, the NCP simulation did not reproduce any of the eastward propagating structures but only westward propagating precipitating systems, which were almost not present in reality.

170   In contrast, the CP simulation (Fig. 2b) reproduced very well the location of the longitudinal precipitation maxima and a dry zone at approx. 45° E, which corresponds to the Horn of Africa. The propagating speed of the eastward moving system was overestimated (approx. 1500 km/day). The precipitation maxima of the propagating systems were slightly underestimated except over the western Pacific warm pool where an excellent agreement was achieved. Although larger differences between the CP simulation and GPM observations are still visible between

175   45° W and 90° W, the correspondence between the longitudinal and temporal structures between the GPM and the CP Hovmöller diagrams is improved compared to the NCP simulation.

3.2 Spectra of tropical convection

Another instructive way to study the behaviour of tropical convection is based on wavenumber-frequency spectrum analyses of the top-of-the-atmosphere (TOA) outgoing longwave radiation (OLR). This methodology is explained in Wheeler and Kiladis (1999). In order to optimize the signal-to-noise ratio of the spectrum and to adapt to the high temporal resolution of our model output, we used the TOA OLR fields provided by the NASA Clouds and the Earth's Radiant Energy System (CERES) project (Loeb et al., 2018). Both the observations and the model outputs are available with 1 h time resolution. However, we derived the spectra with 3-h resolution due to the huge amount of data to be processed and our main interest in an analysis of convectively coupled waves with frequencies below 1 month.

Figure 3 displays the results for the antisymmetric (a-c) and the symmetric spectra (d-f) for a latitude range of ±15° around the equator. In the asymmetric spectra of the CERES data, no strong evidence for the n=2 western or eastern inertio-gravity waves (WIGs or EIGs) was found, but the spectra show a weak signal of the n=0 westward mixed Rossby-gravity wave (MRG) and a particularly strong signal of the n=0 EIG, the latter between shallow water equivalent depths in the range of 12–50 m (LINDZEN, 1967). These structures are absent in the NCP simulations (Fig. 3c) whereas a signal of the n=0 EIG is also found in the CP simulations albeit weaker as in the observations. The symmetric spectra derived with the CERES data may reveal some signal of the n = 1 equatorial Rossby wave (ER). Significant are the spectral power of the n=1 WIG and, particularly strong, the n=1 Kelvin wave for shallow water equivalent depths in the range of 12–50 m for periods between 3-30 days and wavenumbers 1-10. Again, the NCP simulations do not reproduce any of these wave structures. In contrast, albeit somewhat weaker in power, the CP simulation reveal the n=1 WIG from approx. -15 - -5 zonal wavenumbers. Particularly significant is the signal of the n=1 Kelvin wave in the CP wavenumber-frequency spectrum although the slope is somewhat steeper and tending more towards effective depths between 25-50 m. This finding may be related to the overestimation of the eastward propagation of precipitation found in the CP Hovmöller diagrams. Despite these deviations, only the CP simulations are able to recover the observation of IGs, MRGs, and Kelvin waves. This is another strong indication of the added value of nearly global CP simulations on the seasonal scale.

3.3 Spatial distribution of cloud and precipitation

It is clear that the combination of resolution and the omission of the parameterization on the CP scale have significant implications on the structure of deep convective clouds and precipitation. Exemplarily we show this for the monthly averages for May 2015 in order to reduce the spatial-temporal averaging of critical structures. The other months show a similar trend as in May 2015 (not shown).

During May 2015, the CERES OLR observation (Fig. 4a) shows strong convection along the tropics between 10° S and 10° N over the Atlantic, Africa, the Indian Ocean, and the Pacific Ocean indicated by the low values of less than 200 W m^{-2}. Over Africa, the CP simulation shows a better agreement with the observations as compared to the NCP simulation with a bias reduction of 10 W m^{-2} to a total bias of 10 W m^{-2}. The same applies to the Indian Ocean basin, where the NCP simulation shows, on average, 16 W m^{-2} less OLR than observed. Over the Atlantic and South America, the cloud coverage is considerably overestimated inside the ITCZ resulting in an OLR bais of 15 W m^{-2} and a strong precipitation bias in this area. It is also worth to note, that the width of the precipitation

bands over the tropical Atlantic is a lot narrower than observed indicating more localized convection. To complement the results obtained by the OLR analysis, we also investigated the surface shortwave downward radiation.

Figure 5 displays the monthly mean SWDOWN flux during May 2015 over the South American continent. Compared to the LSA-SAF observations (Fig. 5a), the NCP simulation shows very low SWDOWN fluxes over the Amazon rainforest with minimum values of less than 30 W m^{-2} while the minimum observed SWDOWN flux over this particular area is $\approx$180 W m^{-2}. Apart from the southern part of brazil, the CP simulation shows a good agreement with the LSA-SAF observations with an overall bias of only 10 W m^{-2} while the bias of the NCP simulation is 52 W m^{-2}. As the NCP simulation does not show an overestimation of precipitation during this particular month over South America, the strong SWDOWN bias could be related to the simulation of shallow clouds inside the Grell-Freitas cumulus parametrization and its interaction with the RRTMG radiation scheme. Apparently, this interaction is much better resolved in case of the CP resolution.

Figure 6 presents the corresponding accumulated precipitation during May 2015 from the Global Precipitation Mission (GPM) level 3 V06B precipitation data set (Huffman et al., 2019) and the CP and NCP simulations. The differences between the model simulations and the GPM retrieval are presented in Fig. 7.

The GPM observations (Fig. 6a) reveal high precipitation amounts over the intertropical convergence zone (ITCZ) at around 5° N over the Eastern Pacific and the Atlantic Oceans. Large precipitation fields over the tropical West Pacific were also observed. The dry subtropical regions range from 10-35° N and 0-30° S. The CP simulation (Fig. 6b) corresponds well with the structures of dry and moist regions in the GPM data set. Except an underestimation of the dryness in the subtropical regions and an overestimation of the precipitation in the ITCZ over the eastern Pacific, a promising agreement is achieved in spite of the lack of any data assimilation efforts (see also Fig. 7a).

In contrast, the NCP simulation (Fig. 6c) strongly overestimates the precipitation over the entire Pacific including the ITCZ and along the northeast coast of South America. Furthermore, the NCP simulation shows a strong wet bias over the Indian Ocean. In addition, the dry zone extending from Africa towards Asia is not well reproduced and the subtropical dry zone over the southeast Pacific is underestimated. Over South America and from India and Eastern Asia over the entire Island archipelago to New Guinea a strong dry bias is detected (Fig. 7b).

In summary, with respect to the spatial structure of the accumulated precipitation during May 2015, the CP simulation clearly outperforms the NCP simulation. Particularly, the precipitation amounts along the ITCZ, over South America, and over the Indian Ocean are much closer to reality. A clear reduction in precipitation bias of the CP simulations with respect to the NCP simulation was found. Whereas the bias of the NCP simulation in the tropics is 28 mm, it is 45 % less in the CP simulation. The RMSE of the CP simulation in the tropics is 181 mm while it increases to 217 mm in the NCP simulation. The pattern correlation is 0.53 in the CP simulation whereas it is 0.44 in the NCP simulation. These results confirm an added value of global simulations on the CP scale with respect to precipitation on the seasonal scale.

Furthermore, in almost all regions, we found an improvement of the simulation of the diurnal cycle of convection and precipitation (not shown). This is a well-known feature of CP over NCP simulations (Schwitalla et al., 2008; Warrach-Sagi et al., 2013; Ban et al., 2014; Fosser et al., 2015; Prein et al., 2015) .

3.4 Spatial distribution of 2-m temperatures and precipitable water

To investigate the large-scale situation throughout the model simulation, the spatial distribution of precipitable water (PW) and 2-m temperatures was investigated. Figure 8 shows the mean temperature bias averaged between April and June 2015 for the 12 UTC (a,c) and 18 UTC time steps (b,d). The reference data set is the operational ECMWF analysis with its sophisticated 4-dimensional variational data assimilation system (https://www.ecmwf.int/en/elibrary/9209-part-ii-data-assimilation).

At 12 UTC, the NCP shows a strong negative temperature bias over Russia, Mongolia, and China while a strong positive temperature bias is present over India and North Africa. This bias is considerably reduced in the CP simulation except over the eastern part of North Africa while, on average, hardly any bias is present over the southern hemisphere. At 18 UTC, the NCP simulation shows a warm bias over the southern hemisphere while the cold bias over Central Asia remains. The strong negative bias over the Saharan desert and the Arabian Peninsula are probably related to a too strong cooling effect in the WRF model over sand surfaces at higher resolution. This effect was also observed in a study of Schwitalla et al. (2019) who investigated the behaviour of different WRF physics combination over the Arabian Peninsula. It is also interesting to note here that although both simualtions are forced by the same SST data set, a constant temperature bias over the Indian and topical Pacific Ocean is present. A reason for this can be the strong overestimation of precipitation in the NCP simulation (see later in section 3.5).

Figure 9 shows the mean PW content averaged between April and June 2015. The ECMWF analysis (Fig. 9a) shows high amounts of PW along the Intertropical Convergence Zone (ITCZ) over the Atlantic and eastern Pacific Ocean as well as over the Indian Ocean and the tropical western Pacific. On average, both WRF simulations tend to underestimate the amount of water vapour throughout the model domain. As this can be inconclusive, the mean values were calculated for different regions and are shown in Table 1.

Area/region	NCP	CP	ECMWF
180° W – 180° E, 10° N – 55° N	24.6	24.3	24.1
180° W - 180° E, 50° S - 10° S	25.7	23.1	22.6
180° W - 180 ° E, 10° S - 10 °N	45.3	45.2	48.3
South America	38.4	37.1	40.3
North Africa	15.4	14.9	14
Australia	26.7	21.5	22.2
Tropical West Pacific	46.1	48.3	51.8

Table 1: Mean precipitable water (PW) content [mm] averaged over different regions. Column one denotes the averaging region followed by the NCP, CP, and ECMWF values.

The Northern Hemisphere, North Africa and the tropical region show only minor differences with respect to the PW content while larger differences between the simulations occur over South America, Australia, and the tropical West pacific. Over the Southern Hemisphere, the average PW content of the CP simulation is close to the analysed value by ECMWF while a bias of 3 mm is present for the NCP simulation. Over South America, the NCP simulation shows lower PW values as compared to the ECMWF analysis. Here, the CP simulation show an even lower PW content which is also reflected in the dry bias in the Amazon Rainforest (Fig. 6). Over Australia, the strong positive

PW bias of the NCP simulation turns into a small negative PW bias on the convection permitting scale without any reflection in the precipitation fields. The amount of precipitable water in the tropical West Pacific is underestimated in both WRF simulation with the CP simulation having a smaller dry bias as compared to the NCP simulation.

3.5 Teleconnection

In order to study teleconnection pattern, an EOF decomposition of the monthly averaged sea level pressure fields was performed. The reference data set was the ECMWF operational analysis. Figure 8 shows the result of the 1st EOF of the six hourly monthly mean sea level pressure.

Figure 10a upl demonstrates that $\approx$65 % of the sea surface pressure fluctuations in the ECMWF analyses can be explained by the correlation pattern shown in the 1st EOF. Correlation maxima are found in the northeastern Pacific, in the Labrador Sea around the southern tip of Greenland, and along the southern subtropical belt. A correlation minimum covers large areas of Asia. The agreement with the 1st EOF of the CP simulation is excellent (Fig. 10b). Despite a slight underestimation of the strength of the correlations, the spatial structure is very similar and $\approx$61 % of the variance are contained in first EOF. In contrast, the 1st EOF of the NCP simulation (Fig. 10c) shows a completely different pattern. A similar structure shows up only in the 2nd EOF explaining just $\approx$37 % of the variance (not shown). Additionally, a test for eigenvalue separation (North et al., 1982) was performed to ensure that eigenvalues are significantly separated which is true for EOF1 and EOF 2. Consequently, these EOF analyses provide strong evidence in the added value of seasonal CP simulations with respect to the representation of teleconnection pattern and an increase of the quality of nearly global forecasts on the CP scale.

4 Summary

Two 5 month long latitude-belt simulation with the WRF-ARW model version 3.8.1 were evaluated at 3 km and 45 km resolution. The model encompasses a domain between 57° S and 65° N. Meridional boundaries are provided by the operational ECMWF analysis and the lower boundary forcing is provided by combining ECMWF and OASTIA SST data. Although meridional boundary conditions are still applied, the model simulation is undisturbed in the west-east direction, being the main large-scale flow direction on the globe.

Different analyses were applied to demonstrate the added value of nearly global CP simulations. Firstly, the organization of tropical convection was studied by means of Hovmöller diagrams. The strong improvement of spatial-temporal pattern as well as the lifetime and propagation speed of tropical convection systems became evident in the CP simulation. Whereas the NCP simulation predicted mainly a westward propagation in strong disagreement with the observations, the CP simulation produced eastward propagating patterns, which were in striking agreement with the GPM data.

Secondly, wavenumber-frequency spectra of the tropical convection and the detection of various wave pattern were derived by the 3-h TOA OLR fields and revealed by Wheeler-Kiladis diagrams. The CP simulations turned out to be much closer to the observations showing the spectral signatures of eastward propagating EIGs and Kelvin waves, whereas these signatures were absent in the NCP simulations. According to studies of Yang and Ingersoll (2013, 2014), who analysed the Madden-Julian Oscillation (MJO; Madden and Julian, 1972) by applying a shallow water model, a WRF model resolution in the range of 5 km or higher is necessary to be able to represent MJO features assuming an effective WRF model resolution of seven times the horizontal resolution (Skamarock, 2004).

Thirdly, the cloud coverage of convective clouds along the tropics was better represented in the CP simulation. The NCP simulation considerably overestimated cloud cover along the tropical Atlantic, Africa and the Indian Ocean.

Fourthly, the spatial precipitation fields integrated during May 2015 were compared with observations based on the GPM level 3 data set. The spatial pattern of tropical precipitation and the sub-tropical dry regions were much better represented in the CP simulation. While Fowler et al. (2016) found a superior performance of the GF cumulus parametrization when compared to the Tiedtke scheme (Tiedtke, 1989) on a 50 km resolution, the application of a different cumulus parametrization can lead to a reduction of the precipitation bias while the weakness of an incorrect spatial distribution still remains (Gbode et al., 2019, e.g.). As computing resources were limited, an additional experiment with the new Tiedtke scheme (Zhang et al., 2011) was performed for February 2015 (not shown). Depending on the region, the precipitation bias is reduced but the OLR values are too high indicating an improper interaction with the applied RRTMG scheme.

Finally, the spatial structure of teleconnection pattern and the explained variances as studied by the EOF of the surface pressure fields was in close agreement between ECMWF analyses and the CP simulations.

Consequently, our results confirm a significant added value of nearly global CP simulation from the sub-seasonal to the seasonal forecast ranges. We attribute these improvements mainly to the elimination of the lateral forcing by coarse global models, the advanced representation of ocean-land-atmosphere feedbacks and heterogeneities as well as to the elimination of the parameterization of deep convection in the CP run. Obviously, the spatio-temporal structure, the lifetime, and even the teleconnections in the global circulation and its interaction with the development and organization of clouds and precipitation are much better maintained in the CP simulations. These coherent structures are destroyed in the NCP simulation by the amplification of errors induced by deficiencies of parameterizations, e.g., the parameterization of deep convection.

The new CP simulation presented in this work strongly supports the development and application of global, km-scale earth system models, which are envisioned for future climate projections, land-atmosphere feedback studies, e.g., within the CORDEX Flagship Pilot Studies, seasonal simulations, and global NWP ensemble forecasts.

Author contributions

Thomas Schwitalla and Volker Wulfmeyer equally contributed to the design and write-up of this study. Thomas Schwitalla set up, performed the simulations, and collected the data. Thomas Schwitalla and Volker Wulfmeyer analysed the added value of the CP simulations concerning the precipitation fields, the Hovmöller, and the Wheeler-Kiladis diagrams, and the teleconnection. Michael Resch contributed to the model design and the realization of the performance of the model runs on the HRLS supercomputer. Thomas Schwitalla realized the model runs on the HRLS supercomputer as well as the coding, tests, and quality control of the model output. Kirsten Warrach-Sagi

10

contributed to the model output analyses, particularly concerning the precipitation fields as well as the Hovmöller diagrams. All authors contributed to the experiment design.

Competing interests

The authors declare no competing interests.

Code availability

The WRF source code can be obtained from http://www2.mmm.ucar.edu/wrf/users/download/get_source.html after registration. Parallel NetCDF with version higher than 1.6.0 is required and can be downloaded from https://trac.mcs.anl.gov/projects/parallel-netcdf. The applied WRF code changes, NCL scripts and the namelist.input file can be downloaded from https://doi.org/10.5281/zenodo.3550622.

Data availability

As some of the simulation data sets are very large, they can be made available by request from the corresponding author. ECMWF analysis data can be obtained from http://apps.ecmwf.int/archive-catalogue/?class=od&stream=oper&expver=1. Aerosol optical depth data for optimizing the radiative transfer calculations can be obtained from http://apps.ecmwf.int/datasets/data/macc-reanalysis/levtype=sfc/. The user's affiliation need to belong to a member state in order to benefit from these data sets. Radiation data from the LANDSAF project are available after registration from https://landsaf.ipma.pt/en/.
The GPM precipitation data sets are available from https://pmm.nasa.gov/data-access/downloads/gpm after registration. . High-resolution SST data from the OSTIA project can be assessed from ftp://ftp.nodc.noaa.gov/pub/data.nodc/ghrsst/GDS2/L4/GLOB/UKMO/OSTIA/v2 and soil texture data used in this study can be downloaded from https://cera-www.dkrz.de/WDCC/ui/cerasearch/entry?acronym=WRF_NOAH_HWSD_world_TOP_SOILTYP. Satellite TOA OLR data from the CERES project can be obtained from https://doi.org/10.5067/Terra+Aqua/CERES/SYN1deg-1Hour_L3.004A .

References

Ban, N., Schmidli, J., and Schär, C.: Evaluation of the convection-resolving regional climate modeling approach in decade-long simulations, J. Geophys. Res. Atmos., 119, 7889–7907, doi:10.1002/2014JD021478, 2014.

Bauer, P., Thorpe, A., and Brunet, G.: The quiet revolution of numerical weather prediction, Nature, 525, 47–55, doi:10.1038/nature14956, 2015.

Bönisch, T., Resch, M., Schwitalla, T., Meinke, M., Wulfmeyer, V., and Warrach-Sagi, K.: Hazel Hen – leading HPC technology and its impact on science in Germany and Europe, Parallel Computing, 64, 3–11, doi:10.1016/j.parco.2017.02.002, 2017.

Bouttier, F., Raynaud, L., Nuissier, O., and Ménétrier, B.: Sensitivity of the AROME ensemble to initial and surface perturbations during HyMeX, Q.J.R. Meteorol. Soc., 142, 390–403, doi:10.1002/qj.2622, 2016.

Bromwich, D. H., Wilson, A. B., Bai, L., Liu, Z., Barlage, M., Shih, C.-F., Maldonado, S., Hines, K. M., Wang, S.-H.,
400   Woollen, J., Kuo, B., Lin, H.-C., Wee, T.-K., Serreze, M. C., and Walsh, J. E.: The Arctic System Reanalysis, Version 2,
       Bull. Amer. Meteor. Soc., 99, 805–828, doi:10.1175/BAMS-D-16-0215.1, 2018.

Donlon, C. J., Martin, M., Stark, J., Roberts-Jones, J., Fiedler, E., and Wimmer, W.: The Operational Sea Surface
       Temperature and Sea Ice Analysis (OSTIA) system, Remote Sensing of Environment, 2012.

Eyring, V., Bony, S., Meehl, G. A., Senior, C. A., Stevens, B., Stouffer, R. J., and Taylor, K. E.: Overview of the Coupled
405   Model Intercomparison Project Phase 6 (CMIP6) experimental design and organization, Geoscientific Model
       Development, 9, 1937–1958, doi:10.5194/gmd-9-1937-2016, 2016.

Fosser, G., Khodayar, S., and Berg, P.: Benefit of convection permitting climate model simulations in the representation of
       convective precipitation, Climate Dynamics, 44, 45–60, doi:10.1007/s00382-014-2242-1, 2015.

Fowler, L. D., Skamarock, W. C., Grell, G. A., Freitas, S. R., and Duda, M. G.: Analyzing the Grell–Freitas Convection
410   Scheme from Hydrostatic to Nonhydrostatic Scales within a Global Model, Mon. Wea. Rev., 144, 2285–2306,
       doi:10.1175/MWR-D-15-0311.1, 2016.

Gbode, I. E., Dudhia, J., Ogunjobi, K. O., and Ajayi, V. O.: Sensitivity of different physics schemes in the WRF model
       during a West African monsoon regime, Theor Appl Climatol, 136, 733–751, doi:10.1007/s00704-018-2538-x, 2019.

Geiger, B., Meurey, C., Lajas, D., Franchistéguy, L., Carrer, D., and Roujean, J.-L.: Near real-time provision of downwelling
415   shortwave radiation estimates derived from satellite observations, Met. Apps, 15, 411–420, doi:10.1002/met.84, 2008.

Grell, G. A. and Freitas, S. R.: A scale and aerosol aware stochastic convective parameterization for weather and air quality
       modeling, Atmospheric Chemistry and Physics, 14, 5233–5250, doi:10.5194/acp-14-5233-2014, 2014.

Hagelin, S., Son, J., Swinbank, R., McCabe, A., Roberts, N., and Tennant, W.: The Met Office convective-scale ensemble,
       MOGREPS-UK, Quarterly Journal of the Royal Meteorological Society, 143, 2846–2861, doi:10.1002/qj.3135, 2017.

420   Heikenfeld, M., White, B., Labbouz, L., and Stier, P.: Aerosol effects on deep convection: the propagation of aerosol
       perturbations through convective cloud microphysics, Atmospheric Chemistry and Physics, 19, 2601–2627,
       doi:10.5194/acp-19-2601-2019, 2019.

Hines, K. M. and Bromwich, D. H.: Simulation of Late Summer Arctic Clouds during ASCOS with Polar WRF, Mon. Wea.
       Rev., 145, 521–541, doi:10.1175/MWR-D-16-0079.1, 2017.

425   Hong, S.-Y.: A new stable boundary-layer mixing scheme and its impact on the simulated East Asian summer monsoon,
       Q.J.R. Meteorol. Soc., 136, 1481–1496, doi:10.1002/qj.665, 2010.

Hong, S.-Y., Park, H., Cheong, H.-B., Kim, J.-E. E., Koo, M.-S., Jang, J., Ham, S., Hwang, S.-O., Park, B.-K., Chang, E.-C.,
       and Li, H.: The Global/Regional Integrated Model system (GRIMs), Asia-Pacific J Atmos Sci, 49, 219–243,
       doi:10.1007/s13143-013-0023-0, 2013.

430   Hovmöller, E.: The Trough-and-Ridge diagram, Tellus, 1, 62–66, doi:10.1111/j.2153-3490.1949.tb01260.x, 1949.

Huffman, G. J., Bolvin, D. T., Braithwaite, D., Hsu, K., and Joyce, R.: NASA Global Precipitation Measurement
       (GPM)Integrated Multi-satellite Retrievals for GPM (IMERG), NASA, Greenbelt, MD, USA, 2019.

Iacono, M. J., Delamere, J. S., Mlawer, E. J., Shephard, M. W., Clough, S. A., and Collins, W. D.: Radiative forcing by long-
       lived greenhouse gases: Calculations with the AER radiative transfer models, J. Geophys. Res., 113, 233,
435   doi:10.1029/2008JD009944, 2008.

Inness, A., Baier, F., Benedetti, A., Bouarar, I., Chabrillat, S., Clark, H., Clerbaux, C., Coheur, P., Engelen, R. J., Errera, Q.,
       Flemming, J., George, M., Granier, C., Hadji-Lazaro, J., Huijnen, V., Hurtmans, D., Jones, L., Kaiser, J. W.,
       Kapsomenakis, J., Lefever, K., Leitão, J., Razinger, M., Richter, A., Schultz, M. G., Simmons, A. J., Suttie, M., Stein,
       O., Thépaut, J.-N., Thouret, V., Vrekoussis, M., Zerefos, C., and the MACC team: The MACC reanalysis: an 8 yr data
440   set of atmospheric composition, Atmospheric Chemistry and Physics, 13, 4073–4109, doi:10.5194/acp-13-4073-2013,
       2013.

Jarvis, P. G.: The Interpretation of the Variations in Leaf Water Potential and Stomatal Conductance Found in Canopies in the Field, Philosophical Transactions of the Royal Society B: Biological Sciences, 273, 593–610, doi:10.1098/rstb.1976.0035, 1976.

445 Jiménez, P. A., Dudhia, J., González-Rouco, J. F., Navarro, J., Montávez, J. P., and García-Bustamante, E.: A Revised Scheme for the WRF Surface Layer Formulation, Mon. Wea. Rev., 140, 898–918, doi:10.1175/MWR-D-11-00056.1, 2012.

Kendon, E. J., Roberts, N. M., Fowler, H. J., Roberts, M. J., Chan, S. C., and Senior, C. A.: Heavier summer downpours with climate change revealed by weather forecast resolution model, nclimate, 4, 570–576, doi:10.1038/nclimate2258, 2014.

450 Kotlarski, S., Keuler, K., Christensen, O. B., Colette, A., Déqué, M., Gobiet, A., Goergen, K., Jacob, D., Lüthi, D., van Meijgaard, E., Nikulin, G., Schär, C., Teichmann, C., Vautard, R., Warrach-Sagi, K., and Wulfmeyer, V.: Regional climate modeling on European scales: a joint standard evaluation of the EURO-CORDEX RCM ensemble, Geoscientific Model Development, 7, 1297–1333, doi:10.5194/gmd-7-1297-2014, 2014.

LINDZEN, R. D.: Planetary waves on beta planes, Mon. Wea. Rev., 95, 441–451, doi:10.1175/1520-
455 0493(1967)095<0441:PWOBP>2.3.CO;2, 1967.

Loeb, N. G., Doelling, D. R., Wang, H., Su, W., Nguyen, C., Corbett, J. G., Liang, L., Mitrescu, C., Rose, F. G., and Kato, S.: Clouds and the Earth's Radiant Energy System (CERES) Energy Balanced and Filled (EBAF) Top-of-Atmosphere (TOA) Edition-4.0 Data Product, J. Climate, 31, 895–918, doi:10.1175/JCLI-D-17-0208.1, 2018.

Madden, R. A. and Julian, P. R.: Description of Global-Scale Circulation Cells in the Tropics with a 40–50 Day Period, J.
460 Atmos. Sci., 29, 1109–1123, doi:10.1175/1520-0469(1972)029<1109:DOGSCC>2.0.CO;2, 1972.

Madec, G.: NEMO ocean engine, Institut Pierre-Simon Laplace (IPSL),, Paris, France, 2008.

Milovac, J., Ingwersen, J., and Warrach-Sagi, K.: Soil texture forcing data for the whole world for the Weather Research and Forecasting (WRF) Model of the University of Hohenheim (UHOH) based on the Harmonized World Soil Database (HWSD) at 30 arc-second horizontal resolution, World Data Center for Climate (WDCC) at DKRZ,
465 doi:10.1594/WDCC/WRF_NOAH_HWSD_world_TOP_SOILTYP, 2014.

MIYAKAWA, T. and MIURA, H.: Resolution Dependencies of Tropical Convection in a Global Cloud/Cloud-System Resolving Model, Journal of the Meteorological Society of Japan. Ser. II, 97, 745–756, doi:10.2151/jmsj.2019-034, 2019.

Miyamoto, Y., Kajikawa, Y., Yoshida, R., Yamaura, T., Yashiro, H., and Tomita, H.: Deep moist atmospheric convection in
470 a subkilometer global simulation, Geophys. Res. Lett., 40, 4922–4926, doi:10.1002/grl.50944, 2013.

Mogensen, K. S., Magnusson, L., and Bidlot, J.-R.: Tropical cyclone sensitivity to ocean coupling in the ECMWF coupled model, J. Geophys. Res. Oceans, 122, 4392–4412, doi:10.1002/2017JC012753, 2017.

Newman, M., Wittenberg, A. T., Cheng, L., Compo, G. P., and Smith, C. A.: The Extreme 2015/16 El Niño, in the Context of Historical Climate Variability and Change, Bull. Amer. Meteor. Soc., 99, S16-S20, doi:10.1175/BAMS-D-17-0116.1,
475 2018.

Niu, G.-Y., Yang, Z.-L., Mitchell, K. E., Chen, F., Ek, M. B., Barlage, M., Kumar, A., Manning, K., Niyogi, D., Rosero, E., Tewari, M., and Xia, Y.: The community Noah land surface model with multiparameterization options (Noah-MP): 1. Model description and evaluation with local-scale measurements, Journal of Geophysical Research: Atmospheres, 116, doi:10.1029/2010JD015139, 2011.

480 North, G. R., Bell, T. L., Cahalan, R. F., and Moeng, F. J.: Sampling Errors in the Estimation of Empirical Orthogonal Functions, Mon. Wea. Rev., 110, 699–706, doi:10.1175/1520-0493(1982)110<0699:SEITEO>2.0.CO;2, 1982.

Prein, A. F., Gobiet, A., Suklitsch, M., Truhetz, H., Awan, N. K., Keuler, K., and Georgievski, G.: Added value of convection permitting seasonal simulations, Climate Dynamics, 41, 2655–2677, doi:10.1007/s00382-013-1744-6, 2013.

Prein, A. F., Langhans, W., Fosser, G., Ferrone, A., Ban, N., Goergen, K., Keller, M., Tolle, M., Gutjahr, O., Feser, F.,
485   Brisson, E., Kollet, S., Schmidli, J., van Lipzig, Nicole P M, and Leung, R.: A review on regional convection-permitting
       climate modeling: Demonstrations, prospects, and challenges, Reviews of geophysics (Washington, D.C. 1985), 53,
       323–361, doi:10.1002/2014RG000475, 2015.

Satoh, M., Stevens, B., Judt, F., Khairoutdinov, M., Lin, S.-J., Putman, W. M., and Düben, P.: Global Cloud-Resolving
       Models, Current Climate Change Reports, 5, 172–184, doi:10.1007/s40641-019-00131-0, 2019.

490   Schwitalla, T., Bauer, H.-S., Wulfmeyer, V., and Warrach-Sagi, K.: Continuous high-resolution midlatitude-belt simulations
       for July–August 2013 with WRF, Geoscientific Model Development, 10, 2031–2055, doi:10.5194/gmd-10-2031-2017,
       2017.

Schwitalla, T., Bauer, H.-S., Wulfmeyer, V., and Zängl, G.: Systematic errors of QPF in low-mountain regions as revealed
       by MM5 simulations, metz, 17, 903–919, doi:10.1127/0941-2948/2008/0338, 2008.

495   Schwitalla, T., Branch, O., and Wulfmeyer, V.: Sensitivity study of the planetary boundary layer and microphysical schemes
       to the initialization of convection over the Arabian Peninsula, Q.J.R. Meteorol. Soc., 67, 25047, doi:10.1002/qj.3711,
       2019.

Skamarock, W., Klemp, J., Dudhia, J., Gill, D., Barker, D., Wang, W., Huang, X.-y., and Duda, M.: A Description of the
       Advanced Research WRF Version 3, NCAR, Boulder, CO/USA, 2008.

500   Skamarock, W. C.: Evaluating Mesoscale NWP Models Using Kinetic Energy Spectra, Mon. Wea. Rev., 132, 3019–3032,
       doi:10.1175/MWR2830.1, 2004.

Stratton, R. A., Senior, C. A., Vosper, S. B., Folwell, S. S., Boutle, I. A., Earnshaw, P. D., Kendon, E., Lock, A. P.,
       Malcolm, A., Manners, J., Morcrette, C. J., Short, C., Stirling, A. J., Taylor, C. M., Tucker, S., Webster, S., and
       Wilkinson, J. M.: A Pan-African Convection-Permitting Regional Climate Simulation with the Met Office Unified
505   Model: CP4-Africa, J. Climate, 31, 3485–3508, doi:10.1175/JCLI-D-17-0503.1, 2018.

Thompson, G., Field, P. R., Rasmussen, R. M., and Hall, W. D.: Explicit Forecasts of Winter Precipitation Using an
       Improved Bulk Microphysics Scheme. Part II: Implementation of a New Snow Parameterization, Mon. Wea. Rev., 136,
       5095–5115, doi:10.1175/2008MWR2387.1, 2008.

Tiedtke, M.: A Comprehensive Mass Flux Scheme for Cumulus Parameterization in Large-Scale Models, Mon. Wea. Rev.,
510   117, 1779–1800, doi:10.1175/1520-0493(1989)117<1779:ACMFSF>2.0.CO;2, 1989.

Vitart, F.: Evolution of ECMWF sub-seasonal forecast skill scores, Q.J.R. Meteorol. Soc., 140, 1889–1899,
       doi:10.1002/qj.2256, 2014.

Warrach-Sagi, K., Schwitalla, T., Wulfmeyer, V., and Bauer, H.-S.: Evaluation of a climate simulation in Europe based on
       the WRF–NOAH model system: precipitation in Germany, Climate Dynamics, 41, 755–774, doi:10.1007/s00382-013-
515   1727-7, 2013.

Wheeler, M. and Kiladis, G. N.: Convectively Coupled Equatorial Waves: Analysis of Clouds and Temperature in the
       Wavenumber–Frequency Domain, J. Atmos. Sci., 56, 374–399, doi:10.1175/1520-
       0469(1999)056<0374:CCEWAO>2.0.CO;2, 1999.

Yang, D. and Ingersoll, A. P.: Triggered Convection, Gravity Waves, and the MJO: A Shallow-Water Model, J. Atmos. Sci.,
520   70, 2476–2486, doi:10.1175/JAS-D-12-0255.1, 2013.

Yang, D. and Ingersoll, A. P.: A theory of the MJO horizontal scale, Geophys. Res. Lett., 41, 1059–1064,
       doi:10.1002/2013GL058542, 2014.

Žagar, N., Honzak, L., Žabkar, R., Skok, G., Rakovec, J., and Ceglar, A.: Uncertainties in a regional climate model in the
       midlatitudes due to the nesting technique and the domain size, J. Geophys. Res. Atmos., 118, 6189–6199,
525   doi:10.1002/jgrd.50525, 2013.

Zhang, C., Wang, Y., and Hamilton, K.: Improved Representation of Boundary Layer Clouds over the Southeast Pacific in ARW-WRF Using a Modified Tiedtke Cumulus Parameterization Scheme, Mon. Wea. Rev., 139, 3489–3513, doi:10.1175/MWR-D-10-05091.1, 2011.

530

535

540

545

Terrain height (m)

-400   1575   3550   5525   7500
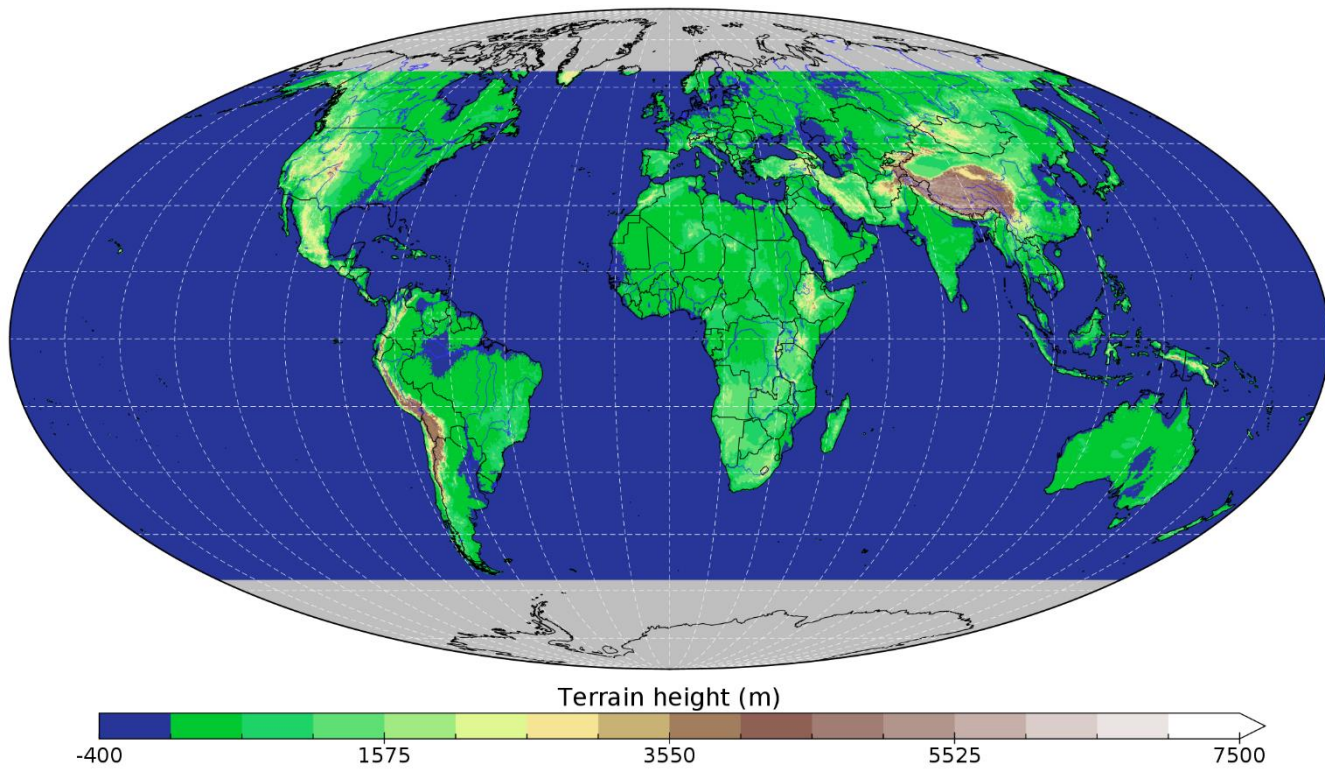
Fig. 1: Applied model domain and terrain height for both the CP and NCP simulations.

550
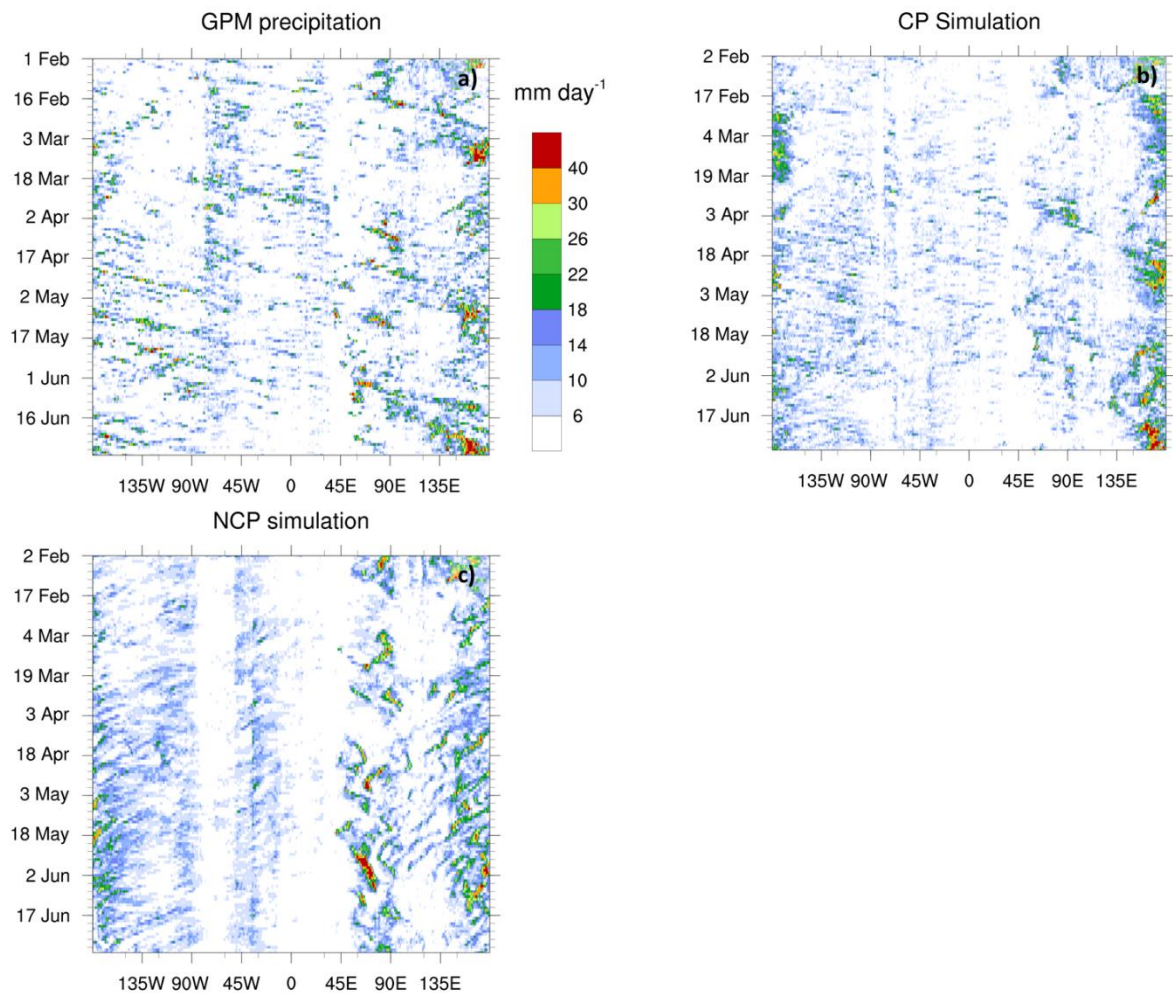
Fig. 2: Time-longitude cross section of the simulated precipitation per day [mm] for the region between 10° S to 10° N. The top row display the GPM precipitation, (b) denotes the CP simulation, and (c) denotes the NCP simulation. The colour bar applies to all plots.

555
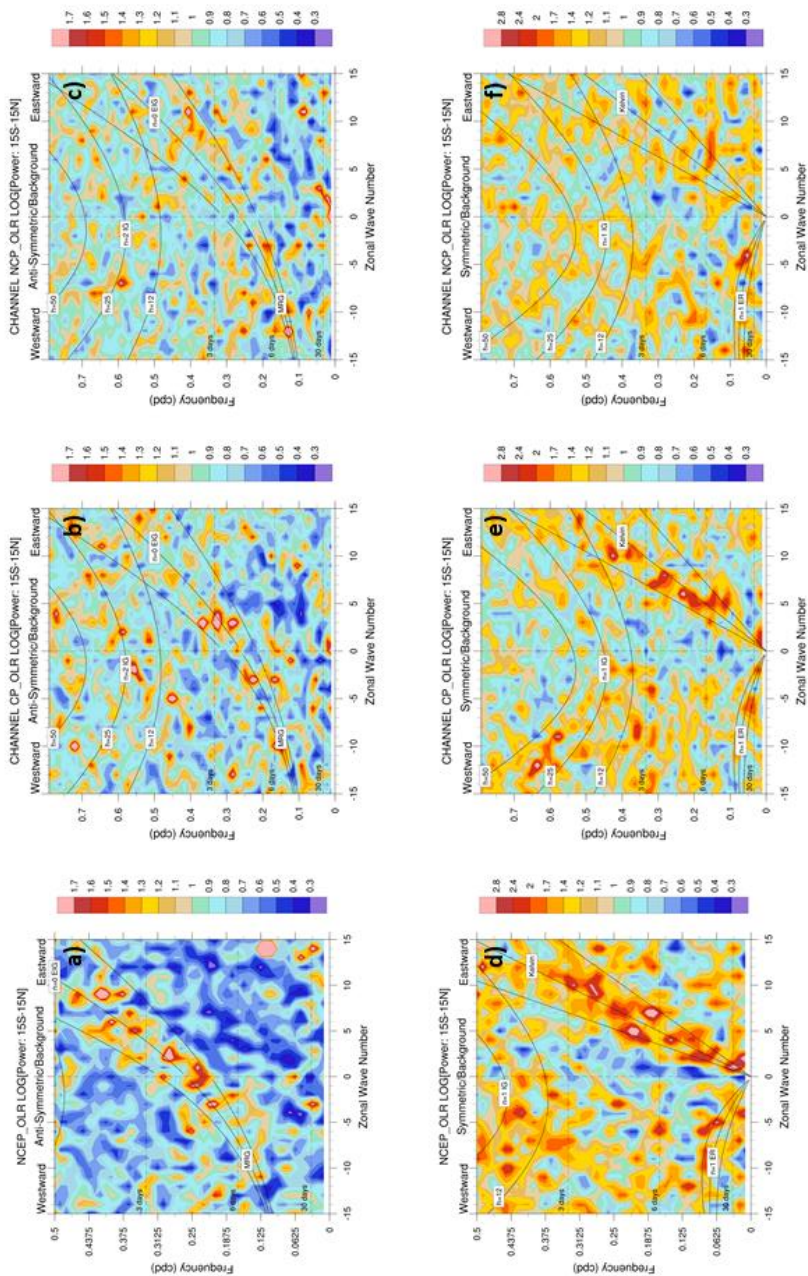
Fig. 3: Wheeler-Kiladis diagrams of the TOA OLR averaged over the latitude belt of ±15° around the equator and sampled with a temporal resolution of 3 h over April-June 2015. (a) and (d): Results achieved with the CERES data, (b) and (e): CP simulations, (c) and (f): NCP resolution. (a)-(c) : antisymmetric spectra, (d)-(f): symmetric spectra.
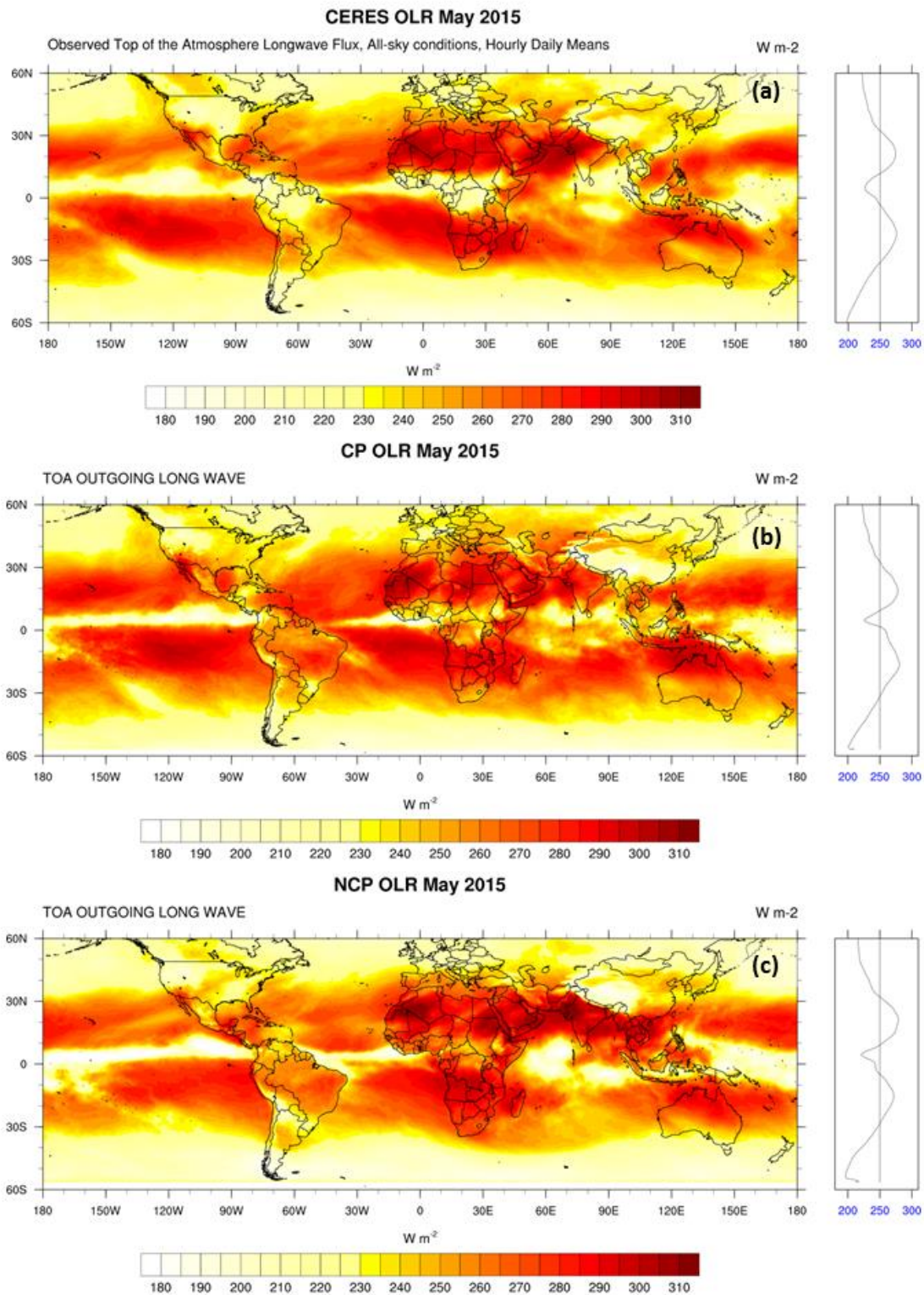
Fig. 4: Monthly averaged Top of the Atmopshere outgoing longwave radiation (OLR) [W m $^-$2] during May 2015 together with the corresponding zonal mean. (a) displays the Clouds and the Earth's Radiant Energy System (CERES) OLR, (b) displays the monthly mean OLR from the CP simulation, and (c) displays the monthly mean from the NCP simulation.

560
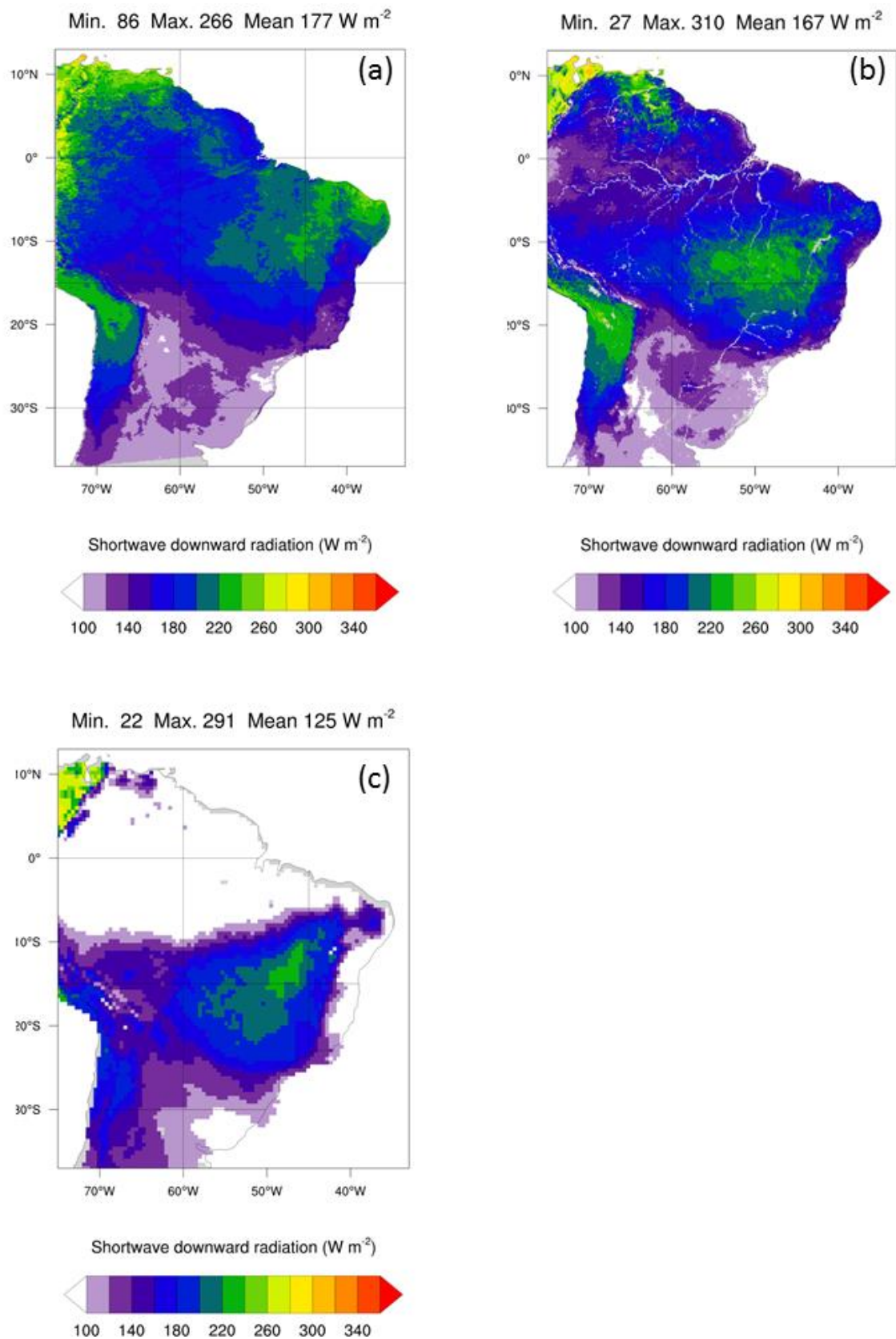
Fig. 5: Monthly averaged surface shortwave downward radiation [W m ⁻²] over South America during May 2015. (a) denotes the LANDSAF satellite observation, (b) denotes the CP simulation, and (c) denotes the NCP simulation. No data are available over the ocean and water areas are masked in the CP and NCP simulations.
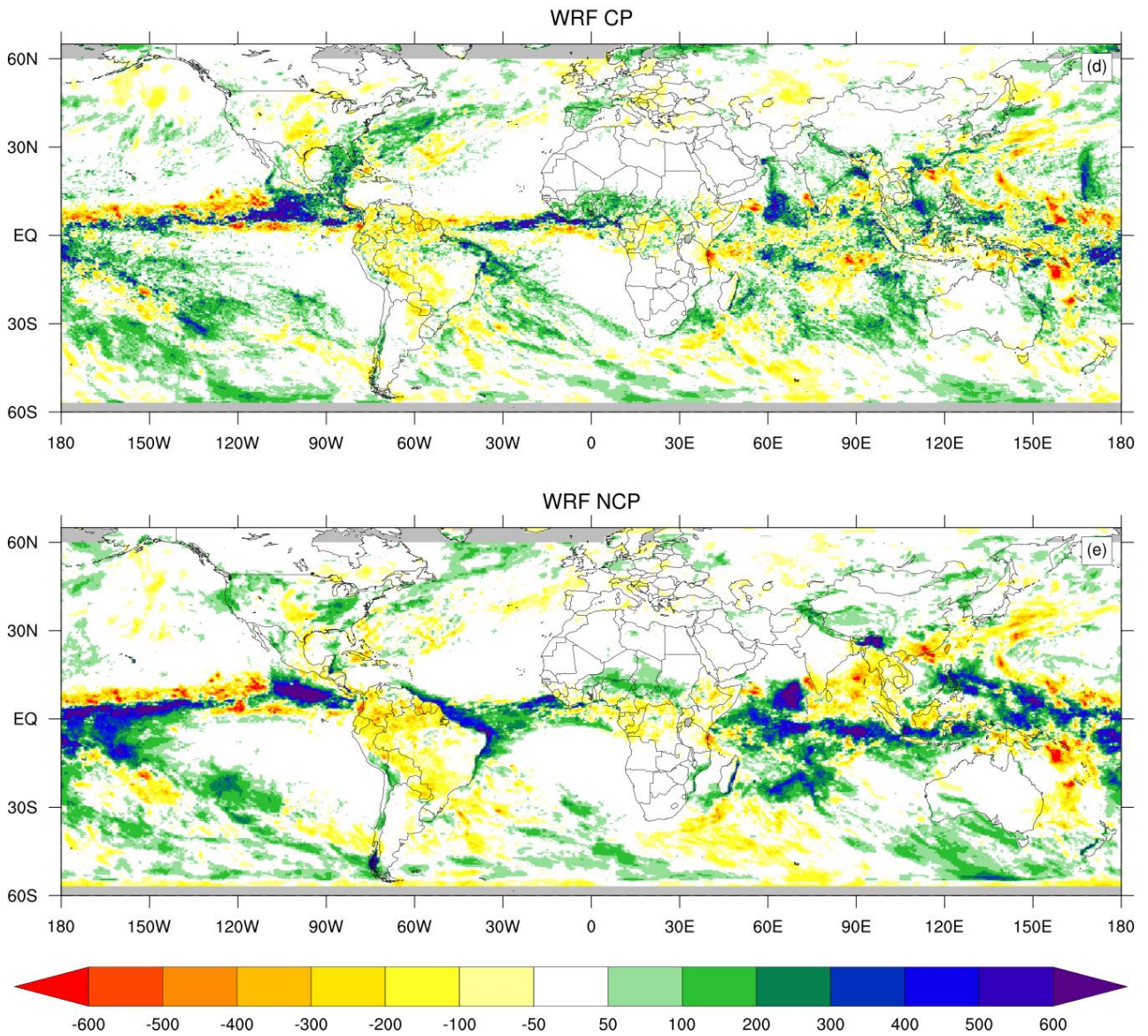
# Accumulated precipitation May 2015
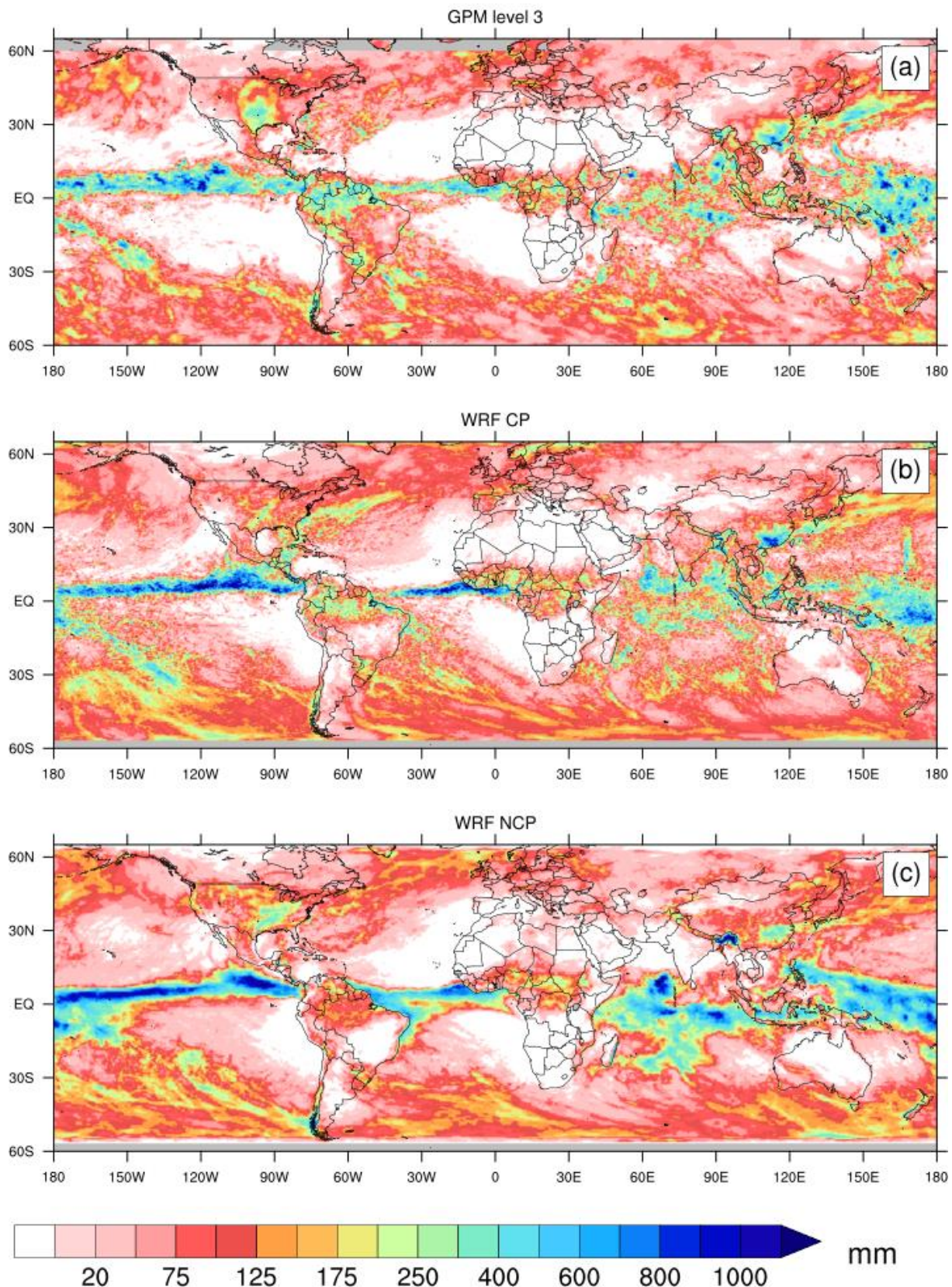
Fig. 6: Accumulated precipitation [mm during May 2015: (a) Global Precipitation Mission (GPM) level 3 data set, (b) CP simulation, (c) NCP simulation. Grey shaded areas indicate lacking coverage in the GPM data or the simulations. The model data are interpolated to the GPM mesh.

Precipitation difference [mm] May 2015
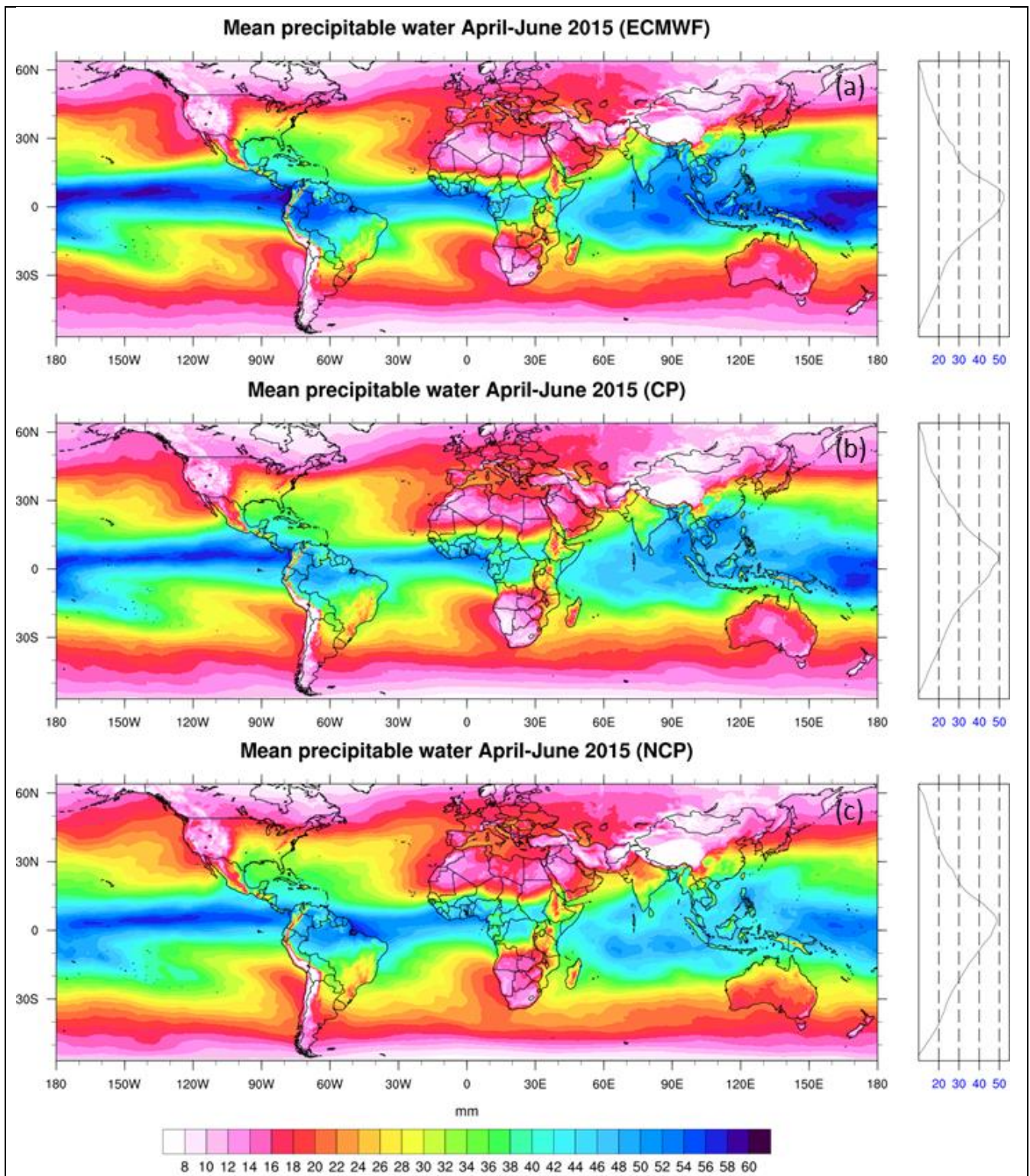
WRF CP

WRF NCP

Fig. 7: Precipitation difference [mm] between CP and GPM (upper panel) and difference between NCP and GPM (lower panel) during May 2015.
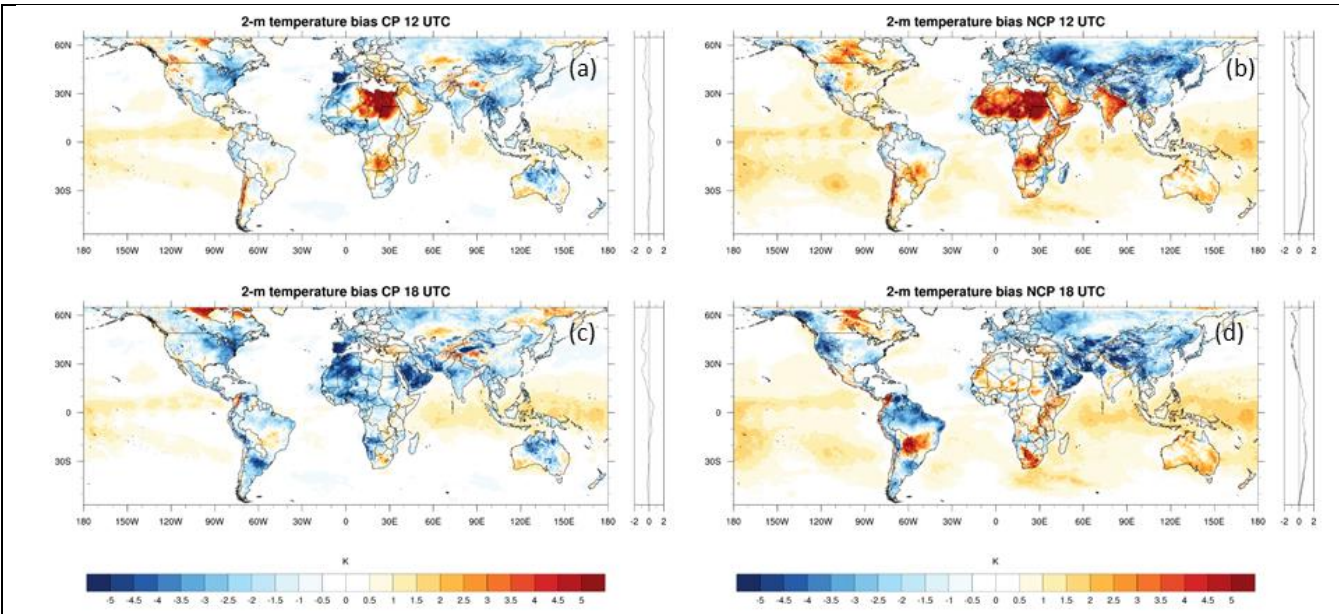
Fig. 8: Mean 2-m temperature bias [K] against the operational ECMWF analysis for the 12 UTC time steps (a,c) and the 18 UTC time steps (b,d) averaged between April and June 2015. On the right side, the zonal mean bias is shown.
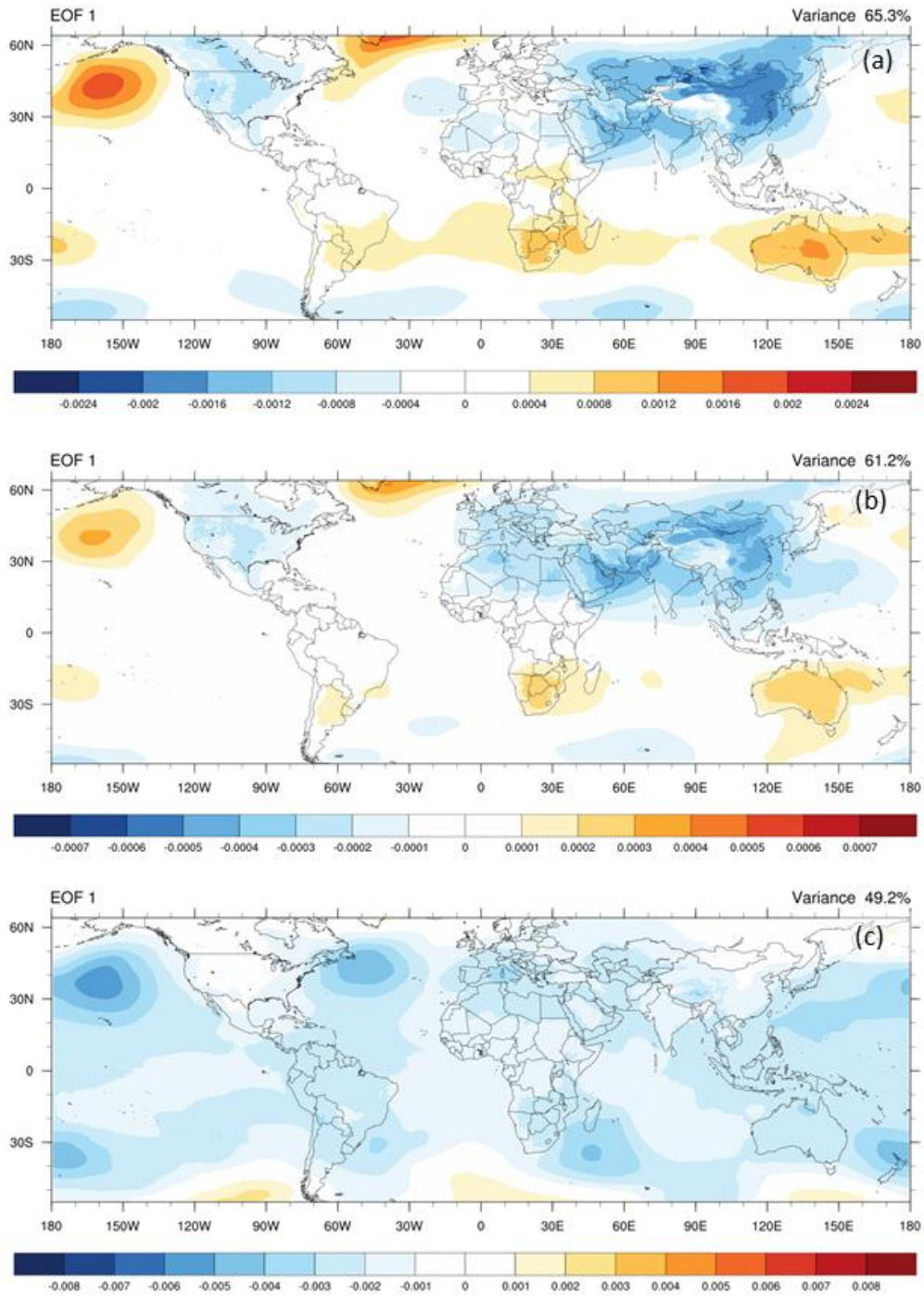
565

Fig. 9: Mean precipitable water (PW) [mm] averaged between April and June 2015. (a) shows the operational ECMWF analysis, (b) the CP simulation, and (c) the NCP simulation. Data are averaged in 6-h intervals to match the ECMWF analysis times. On the right, the zonal mean is shown.

EOF analysis of sea level pressure

Fig. 10: 1st EOF analyses of the monthly mean sea level pressure for the ECMWF operational analysis (a), the CP simulation (b) and the NCP simulation (c) over the whole forecast period. Normalized values are shown and the averaging time steps are 00 UTC, 06 UTC, 12 UTC, and 18 UTC to match the ECMWF analysis time steps.